Infrared Plasmonics with Indium–Tin-Oxide Nanorod Arrays

Shi Qiang Li,[†] Peijun Guo,[†] Lingxiao Zhang,[‡] Wei Zhou,[†] Teri W. Odom,[†,‡] Tamar Seideman,[‡,§] John B. Ketterson,[§] and Robert P. H. Chang[†,*]

[†]Department of Materials Science and Engineering, [‡]Department of Chemistry, [§]Department of Physics, Northwestern University, Evanston, Illinois 60208, United States

ABSTRACT

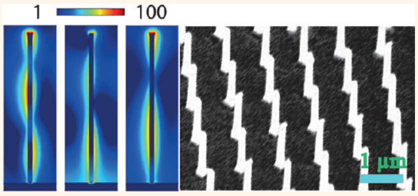

This article reports the study of infrared plasmonics with both random and periodic arrays of indium–tin-oxide (ITO) nanorods (NR). A description is given on the synthesis, patterning, and characterization of physical properties of the ITO NR arrays. A classical scattering model, along with a 3-D finite-element-method and a 3-D finite-difference-time-domain numerical simulation method has been used to interpret the unique light scattering phenomena. It is also shown that the intrinsic plasma frequency can be varied through careful postsynthesis processing of the ITO NRs. Examples are given on how coupled plasmon resonances can be tuned through patterning of the ITO NR arrays. In addition, environment dielectric sensing has been demonstrated through the shift of the resonances as a result of index change surrounding the NRs. These initial results suggest potential for further improvement and opportunities to develop a good understanding of infrared plasmonics using ITO and other transparent conducting oxide semiconducting materials.

KEYWORDS: infrared plasmonics · degenerate semiconductors · transparent conducting oxide · nanorod · sensing · field enhancement

The study of light interaction with nanostructured materials has advanced rapidly as the result of nanofabrication capabilities.[1] A large class of this study has focused on the rich phenomena of light scattered from collections of metallic nanoparticles, such as gold or silver in one, two, or three dimensions. When light is scattered by a metallic nanoparticle, the electric field distributed on its surface can be enhanced by orders of magnitude as modeled by the classical resonance effect, termed localized surface plasmon resonance (LSPR).[2] However, if the collective scattering effects from an array of nanoparticles are taken into account, strongly coupled resonances and propagating modes can be observed.[3,4] Applications of surface plasmon resonance (SPR) include overcoming the diffraction limit in lithography[5] and microscopy,[6,7] high performance photovoltaics,[8] integrated photonic circuits,[9] dynamic optical filters, and chemical and biological sensors.[3]

The frequency range and physical locations of coupled resonances for SPR are determined by the free electron concentration in the metallic nanostructures, their geometry and spatial distribution, as well as their surrounding medium.[10] Gold and silver nanostructures have been studied extensively because the observed LSPR frequency range is in the visible and they are chemically stable to molecular attachment on their surfaces. Gold-based plasmonics has found wide applications, particularly for medical diagnostics.[11] The disadvantage of metals, however, is that their interband transitions are also located at the vicinity of the frequencies of SPR, thus the imaginary component of the dielectric function at resonance is comparable to that of the real part. Consequently, high energy-losses have prevented some of the more promising applications from being realized.[9,12]

In recent years there has been an increasing interest in infrared (IR) plasmonics to further extend the range of applications to include communication and security. To that end the search for new plasmonic materials has expanded to include semiconductors.[12–14] A promising class of materials is the transparent conducting oxides (TCOs). These are degenerate semiconductors with carrier concentrations in the range of 10^{20} to 10^{21} per cm^3. Commonly used TCOs include Sn-doped In oxides (ITO),[14] Al- or Ga-doped Zn oxides, and a mixed family of these oxides. There are several advantages to use TCOs for plasmonics. (1) With the introduction of compositional defects, it is possible to vary the mobility of charge carriers in the material. High mobility will increase the quality factor

* Address correspondence to r-chang@northwestern.edu.

Received for review September 2, 2011 and accepted October 21, 2011.

10.1021/nn203406f

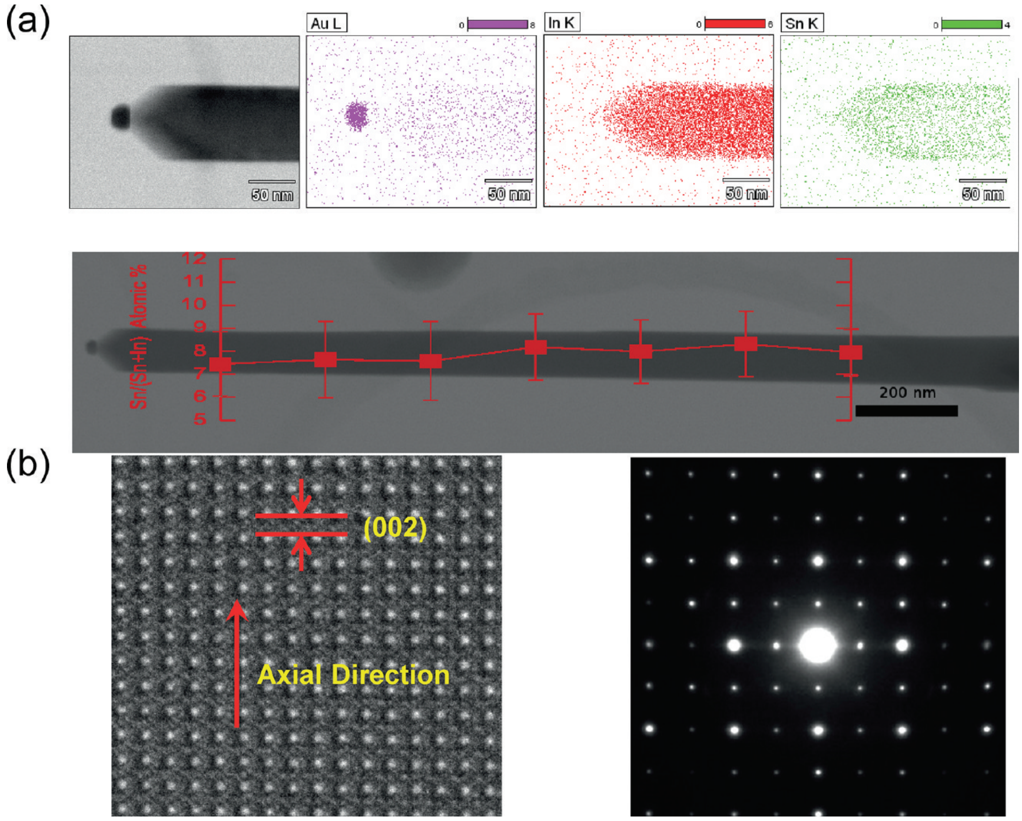

Figure 1. (a) EDS mapping of elements gold, indium, and tin together with a TEM image of an ITO NR. The line scan across the NR plotted in the TEM image shows that the atomic percentage of tin to the sum of tin and indium is 8%. (b) HRTEM micrograph of ITO NR and the corresponding diffraction pattern taken from [001] zone axis.

of a device.[15] (2) Both the charge density and the electron mobility of TCOs can be independently tuned through a large range (∼one decade) *via* processing. This control of plasmon parameters will allow improved understanding of both the basic science and the design of plasmonic devices in the IR. (3) For sensing applications, analyte detection sensitivity should be improved in the IR region. (4) Because of the absence of interband transitions in these TCOs, it has been shown that the imaginary part of the dielectric function is about a factor of 3 or 4 smaller than in the case of silver.[15] Recently, a group at NCSU has published a series of papers on plasmonic phenomena with ITO films.[16−19] Their results have clearly demonstrated the potential for future advancement of TCO materials in plasmonic research. An important future application will be in optical communication, where information can be processed through the integration of IR plasmonic devices with Si and/or compound-semiconductor circuits, and that is then transmitted through optical fibers.[6,7,9,12]

The purpose of this article is to report on a study of light interaction with random and ordered arrays of ITO NRs. Detailed discussions are given in the following sequence: The ITO NR fabrication and characterization are described first. This is followed by a discussion on the connection between random ITO NR density variation and optical properties. Next, it is shown how the ITO NR carrier concentration can be adjusted through processing. Following this, the results of a study on the periodic ITO-NR arrays, with comparison between their optical properties and finite-element-method (FEM) simulations are provided. Finally, a proof-of-concept study of dielectric sensing using an ITO-NR array is presented.

RESULTS AND DISCUSSION

ITO NR Fabrication and Characterization. Following the work of Wan *et al.*,[20] ITO NR arrays were grown epitaxially on yttria-stabilized zirconia (YSZ) (100) substrate. YSZ has a cubic fluorite phase with a lattice parameter $a = 5.14$ Å, while ITO has a bixbyite structure (*i.e.*, a supercell of 2 by 2 by 2 fluorite-phase unit-cells),[21] which closely resembles YSZ. Furthermore, the mismatch between the lattice parameter of ITO and that of YSZ is about 1.7%. Thus, YSZ is an ideal substrate for heteroepitaxial growth of either ITO film or NRs. To grow ITO NRs, a vapor−liquid−solid (VLS) mechanism was adopted. For this purpose a thin (∼10 nm) layer of gold film (serve as catalyst) was coated on YSZ substrates. During the growth process, high temperature in the furnace caused the gold film to break into nanoparticles on the YSZ substrate surface, and these Au nanoparticles served as templates for the

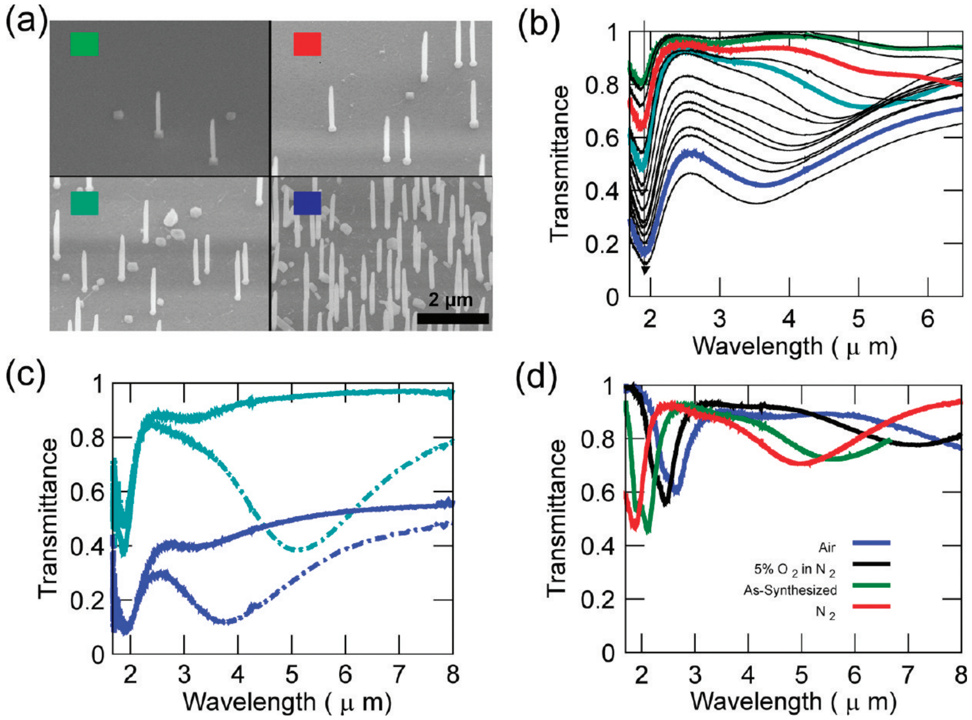

Figure 2. (a) SEM micrographs of NR taken with 30° tilt. The density of rods increases from 5 × 10^6 to 5 × 10^8 NRs/cm^2 from left to right. (b) The transmittance curves of NR arrays taken with an FTIR microscope for a series of NR densities. They were measured with unpolarized light. The sample was annealed in a nitrogen environment before the measurements. Four color-coded curves correspond to the SEM micrographs shown in panel a. The arrow in the graph indicates the increasing density of NRs. (c) Transmittance spectra of two sets of arrays with different NR densities as shown in panel a. Aqua curves are for an array with 1.7 × 10^8 rods/cm^2 and blue curves are for one with 5 × 10^8 rods/cm^2. The dashed curves are measured with *p*-polarized light, whereas the solid curves are measured with *s*-polarized light. (d) The transmittance curves of NR array annealed in air, 5% oxygen, and nitrogen gas along with that of as-synthesized array.

nucleation and subsequent growth of vertically aligned (but randomly distributed) ITO NRs. The typical NR diameter is from 100 to 200 nm determined by the size of the gold catalyst, and its height ranges from a few to 6 μm depending on the growth time and catalyst size. The details of NR patterning and parameters of NR growth are provided in the Methods/Experimental section.

A sufficient amount of tin in the ITO-NRs is important to ensure that they would conduct. High-resolution transmission electron microscopy (HRTEM) along with X-ray energy dispersive spectroscopy (EDS) was used to characterize the crystallinity and the composition of the NRs. Figure 1a shows a transmission electron microscopy (TEM) image of a NR. Three elements of the NR were mapped along the NR length: gold, indium, and tin. As shown in Figure 1a, gold is mainly located at the tip of the NRs, consistent with the VLS growth mechanism. Both indium and tin are identified throughout the NR. Shown together with the TEM images, the EDS line scan along the NR quantifies the doping level of tin to the sum of indium and tin as 8%; the composition is homogeneous along the length of the NR. The difference between the size (~30 nm) of gold tip and the diameter of the NR is shown clearly in Figure 1a. Except at the tip of the NR, its diameter does not vary much from top to bottom. HRTEM images and selected area electron diffraction (SAED) patterns are shown in Figure 1b. It is observed that the NR is single crystalline, and that NRs always grow along the [001] direction, as indicated by the arrow in the HRTEM image. The lattice spacing measured from the image is around 0.5 nm, consistent with that of the (002) plane, which is half the length of the lattice constant of ITO (1.01 nm).

Random ITO NR Density Variation and Optical Properties. Random ITO NR arrays with different rod densities were successfully fabricated by controlling the density of gold seeds, as shown in Figure 2a. The NRs shown here are monodispersed with a typical diameter around 100 and 2600 nm in height. For these samples, the NRs are isolated from each other and there is no ITO layer between them. To ensure this was the case, reactive ion etching (RIE) with a mixture of methane and hydrogen gases was used to remove any ITO in between the NRs. Transmittance spectroscopy was used in this experiment for optical characterization of the ITO NR arrays. Figure 3a shows a schematic diagram of Fourier-transform-infrared-spectroscopy (FTIR) microscope used to collect spectra in the wavelength range from 1667 nm to 20 μm. This microscope uses a cassegrain objective to focus the light onto a small

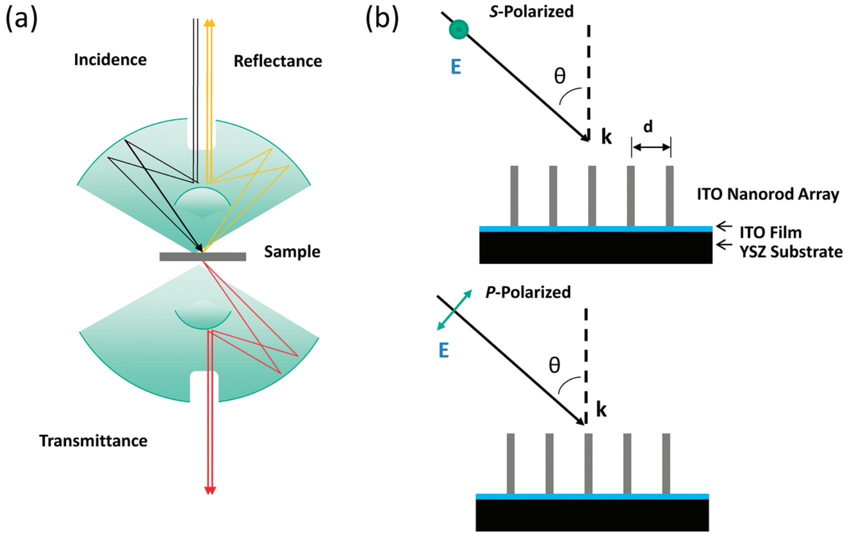

Figure 3. (a) A simplified schematic diagram of the cross-section view of the optical path in the FT-IR microscope used in the experiments. (b) A side view illustrating the interaction of the polarized light with the NR arrays. The angle of incidence θ is 37° with some dispersion.

spot, which greatly enhances the signal and spatial resolution. Furthermore, the focusing path of the light is fixed at an incident angle of 37° to the sample normal. This geometry allows the introduction of a *p*-polarized light component (*i.e.*, *E*-field component in the plane of incidence), and it also allows the analysis of aligned NRs as shown in Figure 3b. The polarization of light was achieved by an asymmetrical light-path through the cassegrain objective and the usage of a polarizer.

The FTIR transmittance measurement was performed on the NR arrays with varying densities (5×10^6 to 5×10^8 NRs/cm^2), as shown in Figure 2b. An absorption peak was observed at around 2 μm for all rod densities. This absorption peak increases in magnitude with increasing NR density without any shift in wavelength, as indicated by the arrow in Figure 2b. The line shape of the peak which closely resembles a doublet is due to the square shape of the NR and this is accurately reproduced by our finite-difference-time-domain (FDTD) simulation results (see Supporting Information S-2). The scanning electron microscope (SEM) pictures in Figure 2a show four different densities of NRs, each is labeled with a different color code that corresponds to a transmission spectrum as plotted in Figure 2b. Furthermore, it is noted that the transmission resonances at wavelength region beyond 4 μm blue-shift as a function of rod density.

To understand the transmission results in Figure 2b, a classical ellipsoidal model is used to gain insight into the relative positions of the two dipole modes involved, the one along the axial direction of the rod (longitudinal mode) and the other, perpendicular to it (transverse mode). Since the aspect ratio of the NRs is 1/26 (100 nm to 2.6 μm) and the spacings of the NRs are all greater than 300 nm on average, dipole moment contribution to the transmission effects will be dominant, so the finer details of the NRs, such as the square-shape, tapering at the tip of the rod, interaction between the base of rod and substrate can be ignored. These details will only contribute significantly to higher order modes.[22] According to the ellipsoidal model, which is an extension of Mie theory, the resonance frequency of the two fundamental modes for isolated spheroids can be determined simply by the plasma frequency and the aspect ratio of the two axes,[10] with the following relationships:

$$\omega_{\mathrm{r},\,(\mathrm{t},\,\mathrm{l})} = \sqrt{\frac{{\omega_\mathrm{p}}^2}{\varepsilon_\infty + \frac{1-L_{(\mathrm{t},\,\mathrm{l})}\varepsilon_\mathrm{d}}{L_{(\mathrm{t},\,\mathrm{l})}}}};\ \omega_\mathrm{p} = \sqrt{\frac{ne^2}{\varepsilon_0 m*}} \quad (1)$$

$$L_\mathrm{l} = \frac{1-e^2}{e^2}\left(-1+\frac{1}{2e}\ln\frac{1+e}{1-e}\right) \quad (2)$$

$$e^2 = 1-\left(\frac{b}{a}\right)^2 \quad (3)$$

$$1 = 2L_\mathrm{t}+L_\mathrm{l} \quad (4)$$

where ε_0 is the permittivity of free space, m^* is the effective mass of electrons in ITO, ε_∞ is the high-frequency permittivity of the ITO (the value used in these calculations is 3.95),[23] e is the elementary charge and ε_d is the permittivity of the surrounding medium. In eq 1, the SPR frequency ω_r is written in terms of the plasma frequency ω_p, the shape factor $L_{\mathrm{t,l}}$, ε_∞, and ε_d, where subscript t denotes transverse mode and subscript l denotes longitudinal mode. The shape factor L_l of the longitudinal mode can be calculated from eq 2 and eq 3 through the knowledge of the aspect ratio b/a, where b is the short axis and a is the long axis. The shape factor L_t, for the transverse mode, can be calculated from eq 4.

With the above equations, the frequencies of the two fundamental modes of the NR arrays can be calculated by using the spectra shown in Figure 2b. Typically, ITO would have plasma frequencies between 1 and 2 eV. The shape factor calculated based on eq 3 and eq 4 are: $L_l = 0.004376$ and $L_t = 0.4978$. Hence, the transmission dips at around 2 μm can be assigned as the transverse mode. (This mode was also simulated by FDTD. The spectrum and near field plots are shown in the Supporting Information, Figure S-1.) By substituting the peak frequency and the shape factor into eq 1 and eq 2, the plasma frequency is found to be 1.53 eV. Using this plasma frequency the longitudinal mode is found to be 0.094 eV (or 12.44 μm). Unfortunately, this mode would not be observed because it is beyond the spectral cutoff frequency (defined by the absorption peak of the phonon modes) from the YSZ substrate at 0.1 eV. However, its presence is manifested by the existence of coupled-dipole resonances discussed below and observed in Figure 2b,c. From the transmission spectra shown in Figure 2b, there are broad transmission resonances (dips) in the spectra, and they shift toward shorter wavelength with increasing NR density. Most of the wavelengths of these transmission resonances are longer than 4 μm in the present experiment, but they are shorter than the ones predicted by the above ellipsoidal model. This is because the model considered above does not take into account the interactions of fields among ellipsoids. When an electromagnetic wave interacts with NR arrays, the scattered far-field consists of the sum of the interactive fields generated by the NRs and the incident field. For the NR arrays in this experiment, the interaction can be well described by coupled-dipole interactions.[24−26] For the case of parallel side-by-side dipole coupling, the scattering of electromagnetic wave with polarization parallel by the dipole array has been calculated and simulated in the literature.[4,26] These modeled calculations provide a good interpretation of the current experimental results in terms of the existence of modes and how the coupled modes behave as a function of materials of NRs, their geometry, inter-NR spacing, as well as the complex relations between direction of the incident wave and the observed scattered waves in terms of phase relations and the possibility of observing a negative refractive index of the NR array. As an example, the models predict the observed effects: (1) The mode coupling strength increases as NR spacing decreases, and this leads to the blue-shift of the resonances according to eq 1 and the Drude model (see Figure 2b). (2) Compared with the shift of the longitudinal mode (along the length of NR), only a minor shift is observed for the transverse mode (across the diameter of NR).[27]

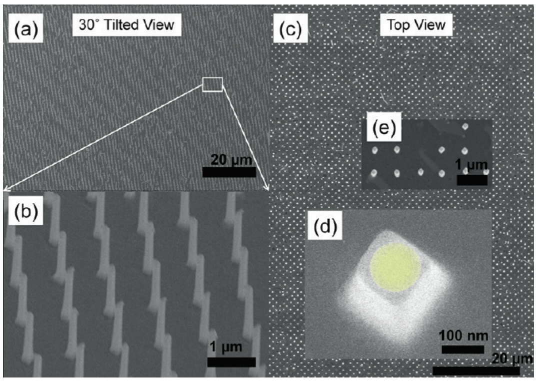

Figure 4. (a) SEM image of a 30° tilted view of a typical patterned NR array with square lattice. (b) Expanded view of a small region in panel a. (c) Top-view image of the array. (d) Expanded view, showing the lateral shape of a rod with a gold particle on top. (e) Expanded view of missing rods in the array. The top-view micrographs are slightly tilted out-of-plane.

Since the NRs are vertically aligned on the substrate in this experiment, it is possible to further extend the study by separating the modes associated with *s*- and *p*-polarized light. It is expected that the longitudinal dipole modes would only be excited by the *p*-polarized light and not by *s*-polarized light. The transmission measurements were thus performed with polarized light on arrays of two different densities as shown in Figure 2c. For *p*-polarization, the denser array has its broad peak at shorter wavelength compared to the less dense array. For *s*-polarization, both arrays do not have any absorption peak beyond 3000 nm. Thus the peak observed for *p*-polarized measurements can be attributed to the coupling of longitudinal modes. No wavelength shift of the peaks occurring at around 2 μm was observed with variation of the NR density and light polarizations.

Adjusting ITO Carrier Concentration. One of the major advantages of TCOs is that the carrier concentration can be varied by the amount of doping and/or by postprocessing control. The latter is studied and presented here. In the case of ITO there are several routes for generating free electrons[28] *via* postsynthesis annealing:

$$2\mathrm{In_{In}}^{\times} + 2\mathrm{SnO_2} \rightarrow 2\mathrm{Sn_{In}}^{\cdot} + 2e' + \mathrm{In_2O_3} + \frac{1}{2}\mathrm{O_2(g)} \quad (5)$$

$$(2\mathrm{Sn_{In}} \cdot \mathrm{O}_i'') \rightarrow 2\mathrm{Sn_{In}}^{\cdot} + 2e' + \frac{1}{2}\mathrm{O_2(g)} \quad (6)$$

$$\mathrm{O_O}^{\times} \rightarrow \frac{1}{2}\mathrm{O_2(g)} + \mathrm{V_O}^{\cdot\cdot} + 2e' \quad (7)$$

Equations 5−7 are written in Kröger−Vink notations.[29] All three routes involve the generation of oxygen gas. Consequently, by annealing ITO in a reducing atmosphere or low ambient oxygen partial pressure (such as vacuum or inert gas environment), it is expected that

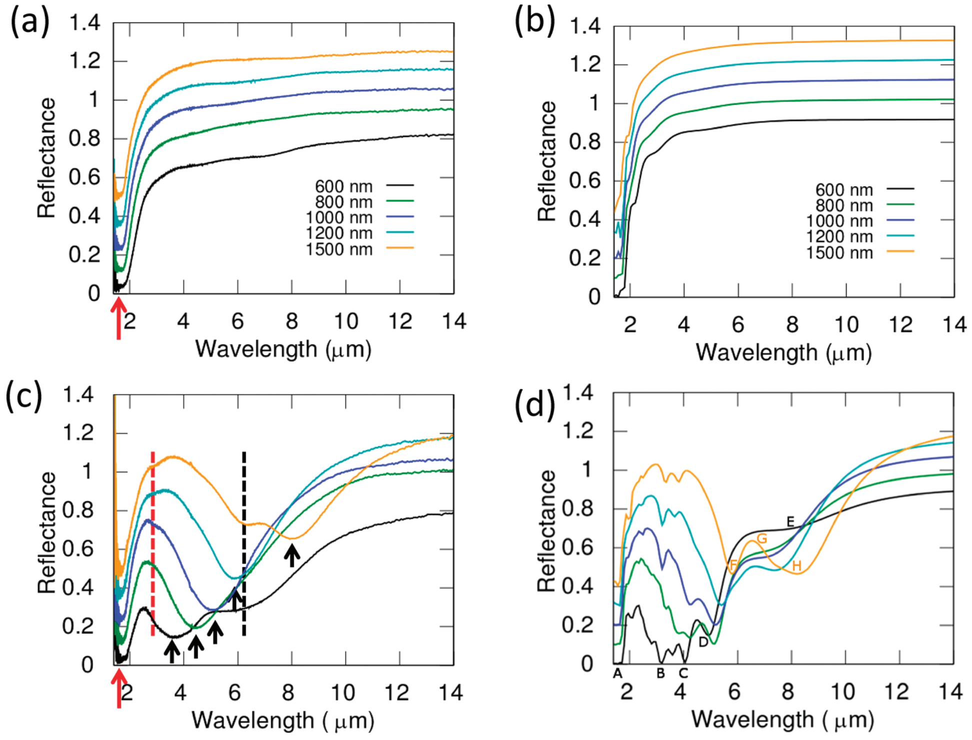

Figure 5. Reflectance measurements of patterned arrays with polarized light sources. (a) Experimental spectra with *s*-polarized light. (b) FEM simulation corresponding to the spectra in panel a. (c) Experimental spectra with *p*-polarized light. (d) FEM simulation corresponding to the spectra in panel c. Spectra in each plot are offset by 10% reflectance from each other for the clarity of representation.

oxygen vacancy formation is preferred and thus leads to higher free-electron concentration. On the other hand, annealing in an environment with high oxygen partial pressure will reduce the electron concentration. The change of carrier concentration, n, will directly alter the plasma frequency of the ITO.

To demonstrate the tunability of plasmonic resonances through carrier concentration adjustment, samples shown in Figure 2a were annealed at an environment of 5% oxygen balanced by nitrogen. All of the peaks shifted significantly, as shown in Figure 2d. The peak at 2210 nm shifted to 2480 nm and the broad peak at 5600 nm shifted to 7000 nm. This is in accordance with decreased carrier concentration by annealing at higher oxygen partial pressure environment, and the resonant frequencies of SPR and intercoupling SPR are directly controlled by the plasma frequency. When air was used as the environmental gas for annealing, the plasma frequency was reduced further (shown as the blue curve in Figure 2d). In contrast, when the ITO NRs were annealed in an inert atmosphere, such as N_2, the peaks were blue-shifted (shown as the red curve in Figure 2d). This is consistent with increasing carrier concentration.

Two different methods can be used to obtain plasma frequency from the experimental spectra: the ellipsoidal model or the FDTD simulation. It was calculated from FDTD that the corresponding plasma frequencies are 1.61 and 1.12 eV for the blue curve and the red curve in Figure 2d, while 1.53 and 1.02 eV were obtained from the ellipsoidal model eq 1 for the same curves. The result from FDTD simulation will be used for calculating the electron concentration, since the ellipsoidal model does not take into account the lateral shape of NR. The corresponding carrier concentration is $n = 7.43 \times 10^{20}$ cm^{-3} and $n = 3.51 \times 10^{20}$ cm^{-3}. Thus, the carrier concentration has been changed by a factor of 2 from these experiments.

Periodic ITO Arrays, Optical Properties, and FEM Simulation. This section focuses on the study of periodic ITO NR arrays by comparing the measured optical resonances with FEM simulations. On the basis of this study it is shown that there are many potential applications for IR plasmonics. As an example, the sensitivity due to index change around the NRs can be used as a sensor.

Patterned arrays with regular spacings are used to allow direct comparison with simulation, which uses periodical boundary conditions. Simulation results, in turn, can help predict and quickly identify the mode coupling among the ITO NRs by mapping the profiles of the near fields around the NRs. Using patterned gold nanoparticles as seeds, NR arrays with different lattice spacings from 600 to 1500 nm were fabricated. The SEM micrographs with (30 degrees) tilted-view of a typical ITO NR array are shown in Figure 4a,b with two different magnifications. In Figure 4c the top view of the NRs is given. The inset in Figure 4d shows the round Au nanoparticle sitting on top of the square-shaped ITO NR. This is consistent with the VLS growth process

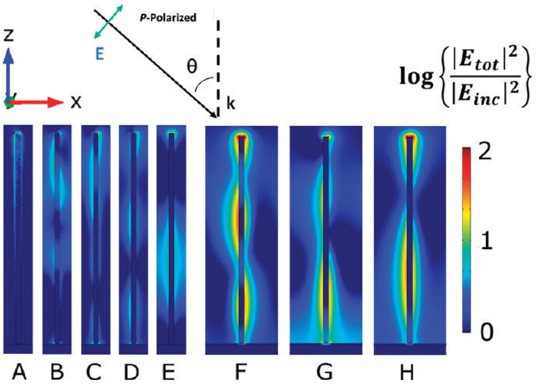

Figure 6. Simulation of the electric field intensity distributions (normalized by the incident electric field intensity) in the *xz* plane of the primitive simulation cell at the reflectance dips for NR arrays with 600 and 1500 nm spacings. A−E, 600 nm spacing; F−H, 1500 nm spacing. The labels A−H correspond to the labels in Figure 5d. The incident light is *p*-polarized, with the E-field in the *xz* plane and an incident angle of 37°. The color scale bar is in log10.

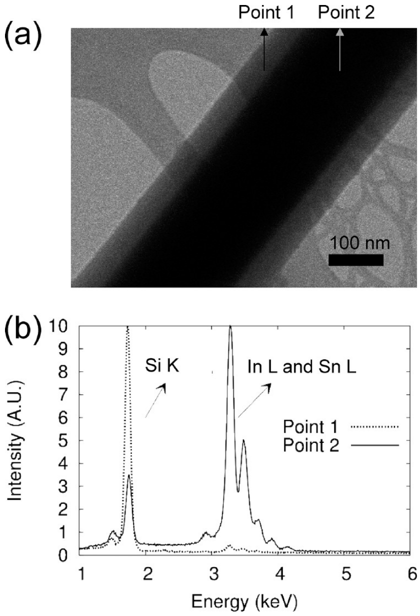

Figure 7. (a) A TEM micrograph of SiO_2-coated NR. (b) The EDS spectra taken from the two points indicated in panel a.

used in the experiment. As can be seen from different perspectives, the NR array pattern is not perfect (*i.e.*, with missing NRs). It has been noted that imperfections in the pattern increase with decreasing inter-NR spacing. Improved fabrication and patterning process are currently under design and development. In Figure 4e the absence of NRs in a typical region of a NR array is shown. These patches of missing NRs along with electronic defects in NRs (*e.g.*, recombination sites) can cause discrepancy when the experimental results are compared with the ideal model used in the FEM simulation (see discussion below).

For the periodic ITO NR arrays, reflection measurements were carried out and compared with simulations. In this case, a thin layer of ITO was first grown on top of the YSZ followed by the growth of NRs. A schematic of this structure is shown in Figure 3b. In Figure 5a, plots of reflectance as a function of wavelength for a series of NR distributions (4.2 μm height) with spacing ranging from 600 to 1500 nm are shown for *s*-polarized incident light, and in Figure 5c for *p*-polarized incident light. Similar to the case of random NRs described above, only one resonance is observed for *s*-polarization, while for *p*-polarization, additional resonances appear at longer wavelengths, as indicated by the black arrows for each NR separation. Due to the periodic nature of the arrays, the resonances are sharper than those for the random NR arrays, and they shift to the red with increasing inter-NR spacings. Only one resonance is observed, at the short wavelength end of the spectra (Figure 5a, indicated by the red arrow). These results are similar to the random NR

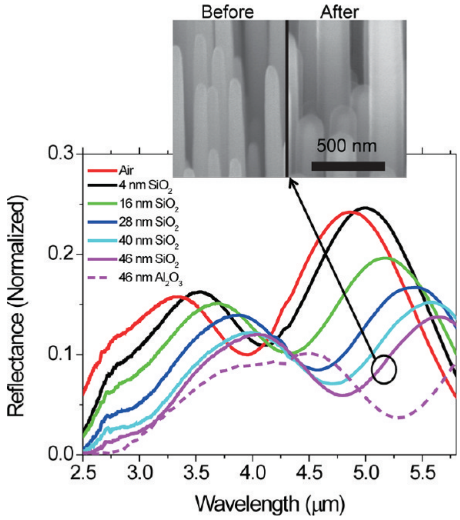

Figure 8. The reflectance spectra of NR arrays coated with different thicknesses of SiO_2 (solid curves). The thickness of the coating varied from 0 to 46 nm. The dashed pink curve is for an array coated with 46 nm Al_2O_3. The SEM micrograph shown in the inset compares the NR array with and without the 46 nm coating.

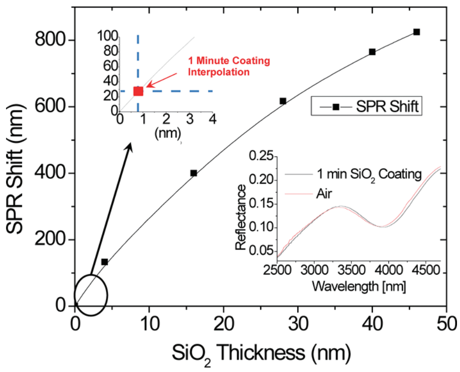

Figure 9. The SPR peak shifts *vs* the coating thickness. The lower inset shows the reflectance curve before and after 1 min of SiO_2 coating. The corresponding thickness was interpolated based on the curve fitted to known thicknesses and is shown in the upper inset.

case discussed above, where coupled resonances are excited only by *p*-polarized light and are shifted with increasing NR spacings. However, in addition to the obvious resonances, several other resonant peaks were observed. For example, for the case of 600 and 1500 nm spacings, these resonances are marked with black and red dashed lines in Figure 5c. Simulation results discussed below predict many resonance peaks, depending on the combination of the NRs height and their mutual separation. For the case of Figure 5c, a third peak is hidden due to the overlapping of the resonances.

To help interpret the experimental results, 3D FEM simulations were performed to calculate the reflectance spectra (following the geometry in Figure 3b) and the corresponding electric field distributions of the patterned NR arrays. (see Supporting Information, section S-2 for detail) A series of simulations was performed for both *s*-polarized and *p*-polarized waves incident on 4.2 μm tall ITO NR arrays with inter-NR spacing ranging from 600 to 1500 nm, as shown in Figure 5b,d. In general, the experimental reflectance measurements (Figure 5a,c) compare well with the simulated results in Figure 5b,d. For the case of *s*-polarization, there is only one resonance (dip) near 1.6 μm for all NR separations. Note, the clear fine structures in the simulated curves (Figure 5b,d) do not appear in the experimental curves (Figure 5a,c). For the case of *p*-polarization (Figure 5c,d), the reflectance curves exhibit more resonances, especially in the simulated curves. To help understand the presence of these extra resonances, near-field profiles for the electric field component are plotted in Figure 6 for the seven resonances labeled from A to G in Figure 5d. From these different profiles, it is reasonable to conclude that the resonances are due to the coupling of dipoles (multipoles) and standing waves as a result of scattering from the ITO NR arrays. Owing to the less-perfect experimental samples, the fine structure features are smeared out. A detailed study of these interesting phenomena is currently underway. The features observed for the IR regime are very similar to those observed for Au nanostructure in the visible range.[30]

Sensitivity to the Refractive Index of Surrounding Media. The basic model of light scattering from a conducting structure indicates that the wavelength location of the resonance is very sensitive to the index of refraction (n) of the medium surrounding the particle.[2] Taking advantage of this unique phenomenon, it is possible to use the ITO NR arrays to sense the index n change of their environment.

To perform such a study, thin layers of SiO_2 ($n \approx$ 1.45) of different thickness were coated around the ITO NRs. Layers of SiO_2 were conformally coated on ITO NRs *via* a modified Stöber method process.[31−33] Using transmission electron microscopy, it is possible to observe the SiO_2 coating on the ITO NR, as shown in Figure 7a. To ensure that the observed coating is SiO_2, EDS measurements were performed at points 1 and 2 in Figure 7a, and the corresponding energy traces are shown in Figure 7b. This measurement clearly indicates the presence of the SiO_2 coating. Following the early procedure, reflectance measurements were carried out for arrays with coatings of different SiO_2 thicknesses (4−46 nm) as shown in Figure 8a. It should be noted that a random ITO NR array was used for this purpose primarily for their smaller NR separation as compared to the NR separations that can be currently fabricated in the ordered array case. From simulation, it is found that smaller NR spacing increases the near field electric field intensity and causes a larger shift in the wavelength of the resonances, thus enhancing the sensitivity. Also plotted in this figure, is the case of an Al_2O_3 coating for comparison. The larger shift for Al_2O_3 is the result of its higher refractive index ($n \approx$ 1.7) compared to SiO_2. The average NR (center to center) separation is about 300 nm and the SEM micrograph of a NR array before and after coating is shown in the inset of Figure 8. At this time the fabrication of a small spacing (less than 400 nm) of an ordered array of NRs is under development. Figure 8 clearly shows the shifts of the traces as a function of SiO_2 layer thickness. A more detailed view of this dependence is given in Figure 9. From this curve, the layer thickness can be determined using a calibrated resonant shift of the reflectance measurement down to very thin layers. It is shown in the insets of Figure 9 that a layer as thin as 1 nm can be measured using this procedure. In principle, it is possible to optimize the sensitivity down to the subnanometer scale. The sensitivity of these NR arrays is roughly 10 times higher in comparison to literature values.[34] Although the detailed study is still ongoing, the increased sensitivity may be attributed to the following causes: (1) Sensitivity increases with resonance wavelengths.[35] Thus SPR infrared sensors should show higher sensitivity as compared to sensors using visible light. (2) Interaction volume is increased by the high-aspect-ratio and closely spaced NRs of the 3-D array structure.[36] (3) Field enhancement is increased and the dispersion relation becomes steeper as a result of an overlapping localized field at small inter-rod distances.[37,38]

CONCLUSION

It has been shown that ITO NR arrays can be used to study plasmonic phenomena in the infrared. A description is given on the synthesis, patterning, and physical properties characterization of the ITO NR arrays. Theoretical models have been adopted to provide physical insight to the observed optical phenomena. 3-D simulations have been performed to provide a more detailed (*e.g.*, fine structures) comparison between theory and experiment. Strong coupling of scattered waves has been observed in the NR arrays and successfully compared with both theoretical models and simulations. Through careful postsynthesis processing, it is shown that the intrinsic plasma frequency can be varied in a controlled way. As an example of application, it is demonstrated that the patterned NR arrays can be used for environment dielectric sensing. These initial results suggest potential for further improvement and opportunities to develop a good understanding of infrared plasmonics using ITO and other TCO semiconducting materials. In depth studies of this topic are currently underway.

METHODS/EXPERIMENTAL

Synthesis of ITO NR Arrays. A single-zone quartz-tube furnace was used for synthesizing ITO NR arrays. In and SnO powders were mixed homogeneously with anatomic ratio of 9 to 1. The mixture was then placed in an alumina crucible located at the center of the furnace, where the temperature was set at 900 °C. A mixture of 0.2% ultra-high-purity (UHP) oxygen gas balanced by UHP nitrogen gas was used as carrier gas and the sources for oxygen in the process. The total gas flow rate was set at 120 sccm. YSZ (100) substrates were used to grow NR arrays, and they were placed at a temperature zone of 800 °C downstream of the alumina crucible. Indium and stannous oxide powder were purchased from Sigma-Aldrich (100 mesh, with 99.99% trace metal basis). All gases used in this study were from Airgas, Inc. Single crystal and double-side polished YSZ (100) substrates were purchased from MTI Corp. YSZ substrates were cleaned with deionized water, acetone, and methanol in sequence. They were then dried using nitrogen gas and cleaned in oxygen plasma cleaner prior to NR and film growth.

Patterning. To create patterned NR arrays, it is critical to ensure that only one NR is grown out of one unit from the pattern. First, a 150 nm thick ITO film was grown on YSZ (100) substrate. Following that, a 3% 950K PMMA in Anisole (950 A3, MicroChem, Inc.) was spin-coated on the substrate (4000 rpm, 60 s). Electron-beam writing was then performed on FEI Quanta 600F environment SEM to write hole (100 nm in diameter) arrays with different pitch distance (from 600 to 1500 nm). The exposed sample was subsequently developed and titanium (1 nm) and gold films (10 nm) were deposited by electron beam evaporation (with Edward Auto 500; gold shot used is 99.99% trace metal basis from Sigma Aldrich.; titanium shot is 99.995% trace metal basis from Ted Pella), followed by lift-off in acetone. The optimum diameter of a gold dot for a single NR growth was found to be 100 nm.

Etching. RIE to remove residual ITO film was done at room temperature using Samco RIE-10NR reactive ion etcher with CH_4 and H_2 (1:4) gases at a pressure of 50 mTorr and a power of 100 W. This process was followed by oxygen plasma clean at 250 W, to remove polymer residue formed.

Annealing. Samples were annealed in the same furnace setup used for growing ITO NRs. All annealing experiments were carried out at 475 °C and a pressure of 350 mTorr. The flow rate was maintained at 100 sccm for all gases used, as described in the text.

Characterizations. The microstructure was characterized using a Hitachi S4800-II SEM. NR growth direction and crystallinity were determined using Joel 2100F TEM and the composition was determined by Hitachi HD2300A scanning TEM equipped with dual EDS detectors. Spectrum Spotlight 300 FTIR microscope from PerkinElmer was used for collecting transmittance and reflectance spectra. The reflectance spectra were normalized with respect to a gold mirror while transmittance spectra were normalized to YSZ substrate. As the response of liquid-nitrogen-cooled mercury−cadmium−telluride detector drifts with time, the absolute reflectance and transmittance were expected to have some deviations. To minimize this deviation, reference spectra were taken at every 500 scans or 5 min, whichever was shorter. Polarization details were described in the main text.

SiO_2 Coating on NRs. A solution of 5 mL of concentrated ammonium hydroxide and 5 mL of water with 20 mL of 2-propanol was prepared. A 0.1 mL portion of tetra-ethyl-ortho-silicate (TEOS) was then added and stirred at room temperature to ensure a homogeneous solution. The NR array was dipped into the solution and held in a water bath at 40 °C for 30 min. After the NR array was removed from the solution, it was then washed with acetone. In this way the coating thickness was precisely controlled, and it increased with processing time.

Simulations. FDTD simulation of the ITO NR array was performed with MEEP,[39] while for isolated NR simulation, a self-developed 3D-FDTD code was employed. FEM simulations were performed on a HP desktop with 24GB memory, enabled by COMSOL Multiphysics RF module. The details of simulation setups were provided in the Supporting Information.

Acknowledgment. The work of S.Q.L., W.Z., L.Z., T.W.O., T.S., and R.P.H.C. were supported by NSF-MRSEC program (DMR-0520513). The work of P.G. was supported by ANSER Center (DOE-DE-SC0001059). The work of J.B.K. was supported by NSF (IGERT-DGE-0801685). SEM, EDS, and TEM were performed at the EPIC facility, and FTIR spectra were measured at KECK II facility. Both facilities are located in NUANCE Center at Northwestern University. NUANCE Center is supported by NSF-NSEC, NSF-MRSEC, Keck Foundation, the State of Illinois, and Northwestern University. RIE and e-beam evaporation were performed at Materials Processing & Microfabrication facility in Northwestern University. The computational resources utilized in this research were provided by Quest cluster system administered by Northwestern University Information Technology (NUIT) unit with Project No. p20194. The authors thank L. J. Lauhon, S. T. Ho, D. Hwang, D. J. Tice, D. B. Buchholtz, C. M. Hseih, B. D. Myers, B. Liu, A. Dhote, X. Chen, S. Li and X. Chen for insightful discussions.

Supporting Information Available: FDTD simulation results of isolated and arrays of ITO NRs, FEM simulation setup, and Drude model parameters are provided. This material is available free of charge *via* the Internet at http://pubs.acs.org.

REFERENCES AND NOTES

1. Barnes, W. L.; Dereux, A.; Ebbesen, T. W. Surface Plasmon Subwavelength Optics. *Nature* **2003**, *424*, 824–830.
2. Jackson, J. D. *Classical Electrodynamics*, 3rd ed.; Willey & Sons: New York, 1999.
3. Anker, J. N.; Hall, W. P.; Lyandres, O.; Shah, N. C.; Zhao, J.; Van Duyne, R. P. Biosensing with Plasmonic Nanosensors. *Nat. Mater.* **2008**, *7*, 442–453.
4. Zhao, L. L.; Kelly, K. L.; Schatz, G. C. The Extinction Spectra of Silver Nanoparticle Arrays: Influence of Array Structure on Plasmon Resonance Wavelength and Width. *J. Phys. Chem. B* **2003**, *107*, 7343–7350.
5. Gramotnev, D. K.; Bozhevolnyi, S. I. Plasmonics Beyond the Diffraction Limit. *Nat. Photon.* **2010**, *4*, 83–91.
6. Kawata, S.; Ono, A.; Verma, P. Subwavelength Colour Imaging with a Metallic Nanolens. *Nat. Photon.* **2008**, *2*, 438–442.
7. Kawata, S.; Inouye, Y.; Verma, P. Plasmonics for Near-Field Nano-Imaging and Superlensing. *Nat. Photon.* **2009**, *3*, 388–394.
8. Atwater, H. A.; Polman, A. Plasmonics for Improved Photovoltaic Devices. *Nat. Mater.* **2010**, *9*, 205–213.
9. Brongersma, M. L.; Shalaev, V. M. The Case for Plasmonics. *Science* **2010**, *498*, 2009–2010.
10. Bohren, C. F.; Huffman, D. R. *Absorption and Scattering of Light by Small Particles*; Wiley & Sons: Weinheim, Germany, 1983.
11. Rosi, N. L.; Mirkin, C. A. Nanostructures in Biodiagnostics. *Chem. Rev.* **2005**, *105*, 1547–1562.
12. Boltasseva, A.; Atwater, H. A. Low-Loss Plasmonic Metamaterials. *Science* **2011**, *331*, 290–291.

13. Luther, J. M.; Jain, P. K.; Ewers, T.; Alivisatos, A. P. Localized Surface Plasmon Resonances Arising from Free Carriers in Doped Quantum Dots. *Nat. Mater.* **2011**, *10*, 361–366.
14. Kanehara, M.; Koike, H.; Yoshinaga, T.; Teranishi, T. Indium Tin Oxide Nanoparticles with Compositionally Tunable Surface Plasmon Resonance Frequencies in the Near-IR Region. *J. Am. Chem. Soc.* **2009**, *131*, 17736–17737.
15. West, P. R.; Ishii, S.; Naik, G. V.; Emani, N. K.; Shalaev, V. M.; Boltasseva, A. Searching for Better Plasmonic Materials. *Laser Photon. Rev.* **2010**, *4*, 795–808.
16. Rhodes, C.; Franzen, S.; Maria, J.-P.; Losego, M.; Leonard, D. N.; Laughlin, B.; Duscher, G.; Weibel, S. Surface Plasmon Resonance in Conducting Metal Oxides. *J. Appl. Phys.* **2006**, *100*, 054905.
17. Franzen, S. Surface Plasmon Polaritons and Screened Plasma Absorption in Indium Tin Oxide Compared to Silver and Gold. *J. Phys. Chem. C* **2008**, *112*, 6027–6032.
18. Franzen, S.; Rhodes, C.; Cerruti, M.; Gerber, R. W.; Losego, M.; Maria, J.-P.; Aspnes, D. E. Plasmonic Phenomena in Indium Tin Oxide and ITO−Au Hybrid Films. *Opt. Lett.* **2009**, *34*, 2867–2869.
19. Losego, M. D.; Efremenko, A. Y.; Rhodes, C. L.; Cerruti, M. G.; Franzen, S.; Maria, J. P. Conductive Oxide Thin Films: Model Systems for Understanding and Controlling Surface Plasmon Resonance. *J. Appl. Phys.* **2009**, *106*, 024903.
20. Wan, Q.; Dattoli, E. N.; Fung, W. Y.; Guo, W.; Chen, Y.; Pan, X.; Lu, W. High-Performance Transparent Conducting Oxide Nanowires. *Nano Lett.* **2006**, *6*, 2909–2915.
21. Bourlange, A.; Payne, D. J.; Jacobs, R. M. J.; Egdell, R. G.; Foord, J. S.; Schertel, A.; Dobson, P. J.; Hutchison, J. L. Growth of Microscale In_2O_3 Islands on Y-Stabilized Zirconia(100) by Molecular Beam Epitaxy. *Chem. Mater.* **2008**, *20*, 4551–4553.
22. Lee, K.-S.; El-Sayed, M. A. Dependence of the Enhanced Optical Scattering Efficiency Relative to That of Absorption for Gold Metal Nanorods on Aspect Ratio, Size, End-Cap Shape, and Medium Refractive Index. *J. Phys. Chem. B* **2005**, *109*, 20331–20338.
23. Granqvist, C. G.; Hultaker, A. Transparent and Conducting ITO Films: New Developments and Applications. *Thin Solid Films* **2002**, *411*, 1–5.
24. Podolskiy, V. A.; Sarychev, A. K.; Narimanov, E. E.; Shalaev, V. M. Resonant Light Interaction with Plasmonic Nanowire Systems. *J. Opt. A: Pure Appl. Opt.* **2005**, *7*, S32–S37.
25. Chaumet, P. C.; Rahmani, A.; Bryant, G. W. Generalization of the Coupled Dipole Method to Periodic Structures. *Phys. Rev. B* **2003**, *67*, 165404.
26. Kullock, R.; Grafström, S.; Evans, P. R.; Pollard, R. J.; Eng, L. M. Metallic Nanorod Arrays: Negative Refraction and Optical Properties Explained by Retarded Dipolar Interactions. *J. Opt. Soc. Am. B* **2010**, *27*, 1819–1827.
27. Tabor, C.; Van Haute, D.; El-Sayed, M. A. Effect of Orientation on Plasmonic Coupling Between Gold Nanorods. *ACS Nano* **2009**, *3*, 3670–3678.
28. Freeman, A. J.; Poeppelmeier, K. R.; Mason, T. O.; Chang, R. P. H.; Marks, T. J. Chemical and Thin-Film Strategies for New Transparent Conducting Oxides. *MRS Bull.* **2000**, *25*, 45–51.
29. Kröger, F. A.; Vink, H. J. Relations between the Concentrations of Imperfections in Crystalline Solids. *Solid State Phys.* **1956**, *3*, 307–435.
30. Zhou, W.; Odom, T. W. Tunable Subradiant Lattice Plasmons by Out-of-Plane Dipolar Interactions. *Nat. Nanotechnol.* **2011**, *6*, 423–427.
31. Stober, W.; Fink, A.; Bohn, E. Controlled Growth of Monodisperse Silica Spheres in the Micron Size Range. *J. Colloid Interface Sci.* **1968**, *26*, 62–69.
32. Ohmori, M.; Matijevic, E. Preparation and Properties of Uniform Coated Colloidal Particles. VII. Silica on Hematite. *J. Colloid Interface Sci.* **1992**, *150*, 594–598.
33. Yin, Y.; Lu, Y.; Sun, Y.; Xia, Y. Silver Nanowires Can Be Directly Coated with Amorphous Silica to Generate Well-Controlled Coaxial Nanocables of Silver/Silica. *Nano Lett.* **2002**, *2*, 427–430.
34. Whitney, A. V.; Elam, J. W.; Zou, S.; Zinovev, A. V.; Stair, P. C.; Schatz, G. C.; Van Duyne, R. P. Localized Surface Plasmon Resonance Nanosensor: A High-Resolution Distance-Dependence Study Using Atomic Layer Deposition. *J. Phys. Chem. B* **2005**, *109*, 20522–20528.
35. Miller, M. M.; Lazarides, A. A. Sensitivity of Metal Nanoparticle Plasmon Resonance Band Position to the Dielectric Environment as Observed in Scattering. *J. Opt. A: Pure Appl. Opt.* **2006**, *8*, S239–S249.
36. Guo, L.; Chen, G.; Kim, D. H. Three-Dimensionally Assembled Gold Nanostructures for Plasmonic Biosensors. *Anal. Chem.* **2010**, *82*, 5147–5153.
37. Kabashin, A. V.; Evans, P.; Pastkovsky, S.; Hendren, W.; Wurtz, G. A.; Atkinson, R.; Pollard, R.; Podolskiy, V. A.; Zayats, A. V. Plasmonic Nanorod Metamaterials for Biosensing. *Nat. Mater.* **2009**, *8*, 867–871.
38. Jain, P. K.; Huang, W.; El-Sayed, M. A. On the Universal Scaling Behavior of the Distance Decay of Plasmon Coupling in Metal Nanoparticle Pairs: A Plasmon Ruler Equation. *Nano Lett.* **2007**, *7*, 2080–2088.
39. Oskooi, A. F.; Roundy, D.; Ibanescu, M.; Bermel, P.; Joannopoulos, J. D.; Johnson, S. G. MEEP: A Flexible Free-Software Package for Electromagnetic Simulations by the FDTD Method. *Comput. Phys. Commun.* **2010**, *181*, 687–702.